Title: Evaluation and Verification of Patient-Specific Modelling of Type B Aortic Dissection

Authors: Chlöe H Armour[1], Baolei Guo[2], Simone Saitta[1,3], Selene Pirola[1], Yifan Liu[2], Zhihui Dong[2], Xiao Yun Xu[1]

Institutions and Affiliations:

[1] Department of Chemical Engineering, Imperial College London, London, SW7 2AZ

[2] Department of Electronics, Information and Bioengineering, Politecnico di Milano, Milan, Italy

[3] Department of Vascular Surgery, Zhongshan Hospital, Institute of vascular Surgery, Fudan University, Shanghai, China

Corresponding Authors:

Prof. Xiao Yun Xu, Department of Chemical Engineering, Imperial College London, London, SW7 2AZ, United Kingdom. Email address: yun.xu@imperial.ac.uk

Prof Zhihui Dong, Department of Vascular Surgery, Zhongshan Hospital, Fudan University, Shanghai, China. Email address: dong.zhihui@zs-hospital.sh.cn

Author Contributions Statement:

CHA – Formal Analysis, Methodology, Visualization, Writing – original draft, Writing – review & editing

BG – Data curation, Writing – review & editing

SS – Formal Analysis, Methodology

SP – Methodology

YL – Data curation, Formal Analysis

ZD – Funding acquisition, Project administration, Supervision

XYX – Conceptualization, Funding acquisition, Project administration, Supervision, Writing – review & editing

Abstract:

Quantitative assessment of the complex hemodynamic environment in type B aortic dissection (TBAD) through computational fluid dynamics (CFD) simulations can provide detailed insights into the disease and its progression. As imaging and computational technologies have advanced, methodologies have been developed to increase the accuracy and physiological relevance of CFD simulations. This study presents a patient-specific workflow to simulate blood flow in TBAD, utilising the maximum amount of *in vivo* data available in the form of CT images, 4D-flow MRI and invasive Doppler-wire pressure measurements, to implement the recommended current best practice methodologies in terms of patient-specific geometry and boundary conditions. The study aimed to evaluate and verify this workflow through detailed qualitative and quantitative comparisons of the CFD and *in vivo* data. Based on data acquired from five TBAD patients, a range of essential model inputs was obtained, including inlet flow waveforms and 3-element Windkessel model parameters, which can be utilised in further studies where *in vivo* flow data is not available. Local and global analysis showed good consistency between CFD results and 4D-MRI data, with the maximum velocity in the primary entry tear differing by up to 0.3 m/s, and 80% of the analysed regions achieving moderate or strong correlations between the predicted and *in vivo* velocities. CFD predicted pressures were generally well matched to the Doppler-wire measurements, with some deviation in peak systolic values. Overall, this study presents a validated comprehensive workflow with extensive data for CFD simulation of TBAD.

Keywords:

Type B Aortic Dissection; Computational Fluid Dynamics; Patient-specific; 4D-MRI; Evaluation and Verification

1. Introduction

Type B aortic dissection (TBAD) is a critical disease of the aorta in which a tear in the inner layer of the descending aortic wall allows blood to flow between the wall layers creating a secondary channel of blood. This results in a true lumen (TL, original aortic channel) and a false lumen (FL, channel within the aortic wall), and often involves multiple additional tears between the TL and FL throughout the thoracic and abdominal aorta [1]. The reduced blood flow in the TL can lead to malperfusion of the aortic branches and eventually organ failure, while the weakened aortic wall can result in complications such as aneurysmal expansion and rupture [2].

There are two therapeutic strategies generally used to treat TBAD – drug based medical therapies or thoracic endovascular aortic repair (TEVAR). While TEVAR is the primary treatment choice for complicated TBAD cases, it remains unclear at the time of diagnosis which uncomplicated patients would benefit from TEVAR. Considerable effort has been made in searching for morphological predictors of disease progressions [3-11] with an aim to identify high risk patients that would benefit from TEVAR. However, these studies did not assess the influence of aortic hemodynamics which may play a critical role in disease progression. Evaluation of hemodynamic metrics under patient-specific conditions can provide additional information that may help clinicians choose the most appropriate treatment for a given patient.

To understand blood flow characteristics in TBAD, numerous studies using image-based computation fluid dynamics (CFD) simulations have been reported over the past decade [e.g. 12-25]. The complexity of simulations has increased as both imaging and computational technologies developed. While early studies tend to employ geometries focusing on the dissected aorta alone, with either no major side branches [14,15,17] or only the aortic arch branches segmented [12,16,21,24], patient-specific geometries including all major side branches are now routinely utilised [13,18,20,23,25]. Several anatomical studies have identified the important role of side branches in FL thrombosis [26,27] and FL expansion [28], hence their inclusion in CFD models is necessary to accurately predict dissection hemodynamics and its association with disease progression. The choice of inlet and outlet boundary conditions also evolved from idealised settings to physiologically accurate boundary conditions. For example, the use of 3-element

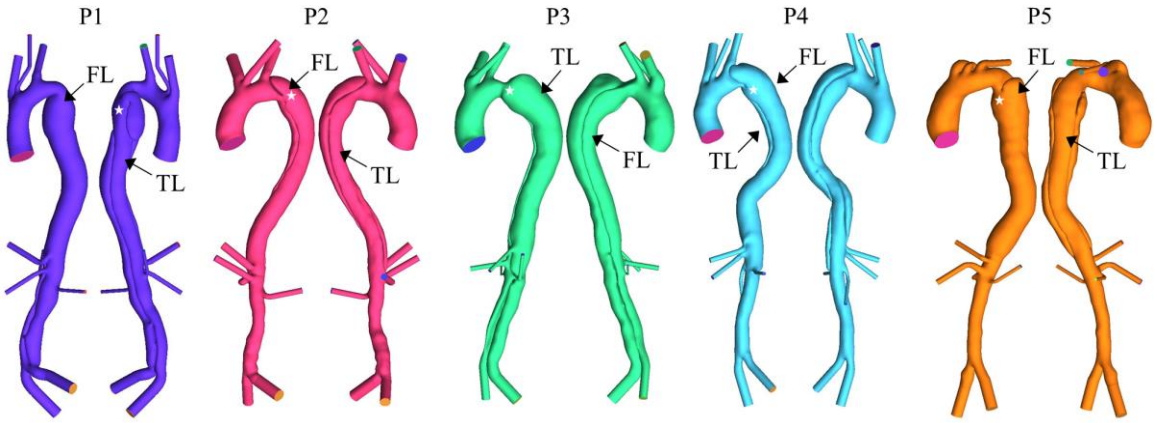

Figure 1: Patient-specific geometric models reconstructed from CT scans. For each model the true (TL) and false (FL) lumen are labelled with an arrow, and the primary entry tear is indicated by a white star. [colour figure]

Windkessel (3EWK) models as outlet boundary conditions [29] and patient-specific 3D inlet velocity profiles derived from 4D-flow MRI [30].

While previous studies have contributed to the development and improvement of methodologies, there is a lack of comprehensive evaluation and verification of the simulation workflow utilising the maximum amount of *in vivo* data available to derive a complete set of optimal patient-specific boundary conditions. This study aimed to present, evaluate and validate such a patient-specific simulation workflow, through detailed qualitative and quantitative analysis of CFD simulations of five TBAD patients compared to *in vivo* data.

2. Methods

Five TBAD patients (P1-P5) from Zhongshan Hospital, Fudan University, Shanghai, were included in this study. For all patients diagnostic CT and 4D-flow MRI scans were available. Geometries of the affected aorta were segmented from the CT scans in Mimics (Materialise HQ, Leuven) through automatic thresholding and manual refinement. CFD models included all major side branches: brachiocephalic (BRAC), left common carotid (LCCA) and left subclavian (LSA) artery, celiac trunk (CEL), superior mesenteric artery (SMA), right (RR) and left (LR) renal, and right (RI) and left (LI) iliac. Each branch was extended by 40 mm to ensure applied boundary conditions did not affect upstream flow. The reconstructed models are shown in Figure 1. Computational meshes were generated using ICEM CFD (Ansys Inc, v15.0), consisting of hexahedral core elements and ten prismatic wall layers. The mesh was refined in complex regions

	P1	P2	P3	P4	P5
Cycle Period [s]	0.658	1.048	0.774	0.942	0.858
Peak Re	3595	3507	3821	4081	4734
Re_c	4643	4656	5280	4330	4469
α	18.6	18.6	21.1	17.3	17.9
Stroke Volume [*mL*]	74	116	117	117	113

Table 1: Key flow parameters of the inlet flow waveform for patients P1-P5. Re - Reynolds number; Re_c - critical Re, equal to 250α [28]; α - Womersley number.

including tears and sharp bends at branches. Mesh sensitivity tests were conducted to ensure mesh independent solutions. For these tests, three meshes were created for each patient model, and using each mesh a transient simulation with a flat inlet velocity profile and 0 pressure outlets was run. The chosen mesh produced differences of <5% in mean and maximum velocity and time-averaged wall shear stress (TAWSS) on selected planes throughout the geometries when compared to a finer mesh. The final meshes selected contained 4.0 million, 4.3 million, 5.6 million, 4.8 million and 5.0 million for P1, P2, P3, P4 and P5, respectively.

For the full CFD simulation time-varying 3-directional inlet velocity profiles were extracted from the 4D-flow MRI data for each patient, using an in-house MATLAB process tool, developed and presented in our previous studies [20,30,31]. Additionally, from the 4D-flow MRI data flow splits to the branches were determined by placing planes at various locations along the aorta and measuring the change in flowrate before and after such planes. Depending on image quality planes were placed between each aortic branch to determine flowrates to the BRAC, LCCA and LSA individually, or planes were placed before and after the aortic branches with flow being distributed between the three branches based on the area of each branch. Flow through the abdominal branches was determined by measuring the change in flowrate at planes before and after the branches and was then distributed based on area. Furthermore, invasive Doppler-wire (DW) pressure measurements were taken during the TEVAR procedure, under general anaesthesia, just before endograft implantation, providing pressure values in the ascending aorta, within the primary entry tear (PET), and at spine vertebrae locations T9, T12 and L1 within both the TL and FL. Catheterization was conducted using a 4-F VER catheter (Cordis, Warren, New Jersey), with a connected pressure transducer. The average pressure for each branch was calculated from the DW curve recorded at the location closest to that branch, with the TL or FL measurement being selected depending on which lumen the branch was perfused by. These

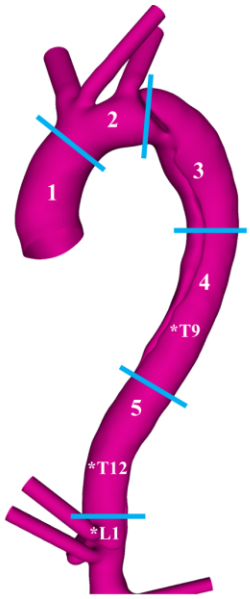

	Location	Description
1	Ascending aorta (AAo)	Inlet to the braceocephalic artery
2	Aortic arch (AA)	Braceocephalic artery to left subclavian artery
3	Proximal descending aorta (Prox-DAo)	Left subclavian artery to vertical DAo
4	Mid descending aorta (Mid-DAo)	Distal Prox-DAo to half the distance to celiac trunk
5	Distal descending aorta (Dis-DAo)	Distal Mid-DAo to celiac trunk

*T9, *T12, *L1 indicate the locations of the thoracic and lumbar spinal points

Figure 2: Definition of regions of the aorta (1-5), distinguished by blue lines on the example aorta, used for analysis. Locations of thoracic and lumbar spinal points T9, T12, L1, used for analysis of pressure, are also indicated. [colour figure]

cycle-averaged pressures along with the 4D-flow derived flow splits were used to calibrate 3EWK parameters for all branches in each patient model following the methodology reported by Pirola et al. [20].

In all simulations the Quemada model was adopted to describe the non-Newtonian behaviour of blood, with model parameters taken from the literature [32]. The flow was assumed to be laminar based on calculations of the peak Reynolds number (Re), Womersley number and critical Re for transition to turbulence reported by Kousera et al. [33]. A summary of these key flow parameters is given in Table 1. The peak Re for P5 was slightly above the critical Re, however, as the values were close the flow was modelled as laminar for computational efficiency. Simulations were run in Ansys CFX (Ansys, v20), a time step of 0.001 s was used throughout, and all simulations were run until a periodic solution was achieved. The final cycle was used for analysis, and results were post-processed using EnSight (Ansys, v20). Analysis included qualitative and quantitative assessment of velocity, flow patterns and pressure throughout the dissection. Additionally, the false lumen ejection fraction (FLEF), defined in equation 1 [34], was measured at the PET.

4D-flow MRI scans were processed using in-house MATLAB tools from which velocities were qualitatively and quantitatively assessed in the same way as the CFD results. For qualitative assessment the data extracted using the MATLAB tool was visualised in EnSight, where the

	P1	P2	P3	P4	P5
AAo diameter[a] [cm]	2.9	3.7	3.6	3.2	3.3
Max DAo diameter[b] [cm]	4.4	3.8	5.2	3.9	4.9
Number of tears	7	5	5	5	2
PET size[c] [cm]	3.2	2.0	2.3	0.9	1.6
LSA to PET distance[d] [cm]	3.1	1.6	1.4	0.9	2.7
Dissection location[e]	LSA-BIF	LSA-SMA	LSA-BIF	LSA-LR	LSA-CEL
Length of dissection[f] [cm]	34.0	28.7	41.6	33.0	23.2
Tortuosity[g]	1.05	1.14	1.13	1.29	1.04

Table 2: Geometric features of patients P1-P5. [a]Ascending aorta (AAo) diameter calculated based on inlet area. [b]Maximum descending aorta (DAo) diameter measured on the axial slices of the CT scans. [c]Primary entry tear (PET) measured as the maximum axial diameter of the tear. [d]Distance measured along the centreline of each 3D model. [e]Start and end point of dissection; LSA - distal to the left subclavian artery; BIF - aortic bifurcation; SMA - superior mesenteric artery; CEL - celiac trunk; LR - left renal artery. [f]Length of dissection measured along the centreline of each 3D model. [g]Tortuosity calculated as the length of dissection along the centreline divided by the straight vertical distance between the start and end of dissection.

velocity results were interpolated onto a finer grid using EnSight's inbuilt volume rendering function. For a detailed comparison of the measured and predicted flow fields the Pearson's correlation coefficient (R) was evaluated to measure the linearity between the CFD and 4D-MRI velocities. For this analysis the CFD data was filtered to extract velocities at the same spatial resolution and coordinates as the 4D-MRI data. R was evaluated in 5 regions of the aorta: ascending aorta (AAo); aortic arch (AA); proximal descending aorta (Prox-DAo); Mid-DAo; Distal DAo (Dis-DAo). A description and definition of these regions can be seen in Figure 2. This is a statistical method that has been employed in previous biomedical studies to assess agreement between 4D-MRI and CFD or experimental velocities [35-37]. From the 4D-flow MRI data, the FLEF was also measured at the PET.

$$FLEF(\%) = \frac{Retrograde\ flow_{Diastolic}}{Antegrade\ flow_{Systolic}} \quad (1)$$

3. Results

3.1. Geometric features

Table 2 reports various geometric features for each patient. Both the AAo diameter and maximum DAo diameter varied among the patients (2.9 - 3.7 cm in the AAo and 3.8 - 5.2 cm in the DAo). All patients had 5 tears in total, with varying sizes of PET (0.9 - 3.2 cm). The dissection began at the LSA in all patients, and extended the full length of the aorta to the bifurcation in P1 and P3, while the TL and FL combined above the CEL in P5, above the SMA in P2 and at the LR in P4.

	Aortic side branch diameter [mm]								
	BRAC	**LCCA**	**LSA**	**CEL**	**SMA**	**RR**	**LR**	**RI**	**LI**
Standard	12.4	7.4	8.5	7.8	8.7	5.2	5.2	12.0	12.0
P1	10.2	5.0	9.0	7.3	5.4	4.4	4.2	13.5	13.4
P2	15.3	10.0	12.3	10.4	9.3	8.5	8.2	13.6	16.5
P3	14.9	8.5	11.5	5.7	7.3	3.2	4.8	11.8	15.1
P4	12.5	7.0	10.4	6.7	6.0	4.8	4.6	12.7	10.7
P5	13.4	7.3	9.5	6.1	8.1	4.2	4.7	15.2	15.1

Table 3: Diameter of each aortic side branch for all patients. Standard branch diameters reported by Du et al. [38] and Uberoi et al. [39] are also given. Branches include brachiocephalic (BRAC), left common carotid (LCCA) and left subclavian (LSA) artery, celiac trunk (CEL), superior mesenteric artery (SMA), right (RR) and left (LR) renal, and right (RI) and left (LI) iliac.

There were also varying levels of tortuosity between the patients, with a near 1 value in P1 and P5 (not tortuous), and the highest value of 1.29 in P4. The diameters for all side branches are summarised in Table 3 which also contains standard diameters for each branch which have previously been reported by Du et al. [38] and Uberoi et al. [39]. It can be seen that the measured diameters do vary between patients and from the standard value for some branches, for example P2 had large diameters in all branches, while individual branches in P1 (LCCA) and P3 (RR) were small compared to other patients and standard values.

3.2. Inlet flow waveforms and measured pressure

Figure 3 shows the inlet flow waveforms extracted from the 4D-flow MRI data, while the corresponding key flow parameters are given in Table 1. Among the patients the cardiac cycle period varied between 0.658 and 1.048 seconds, the peak systolic flow varied between 18.7 and

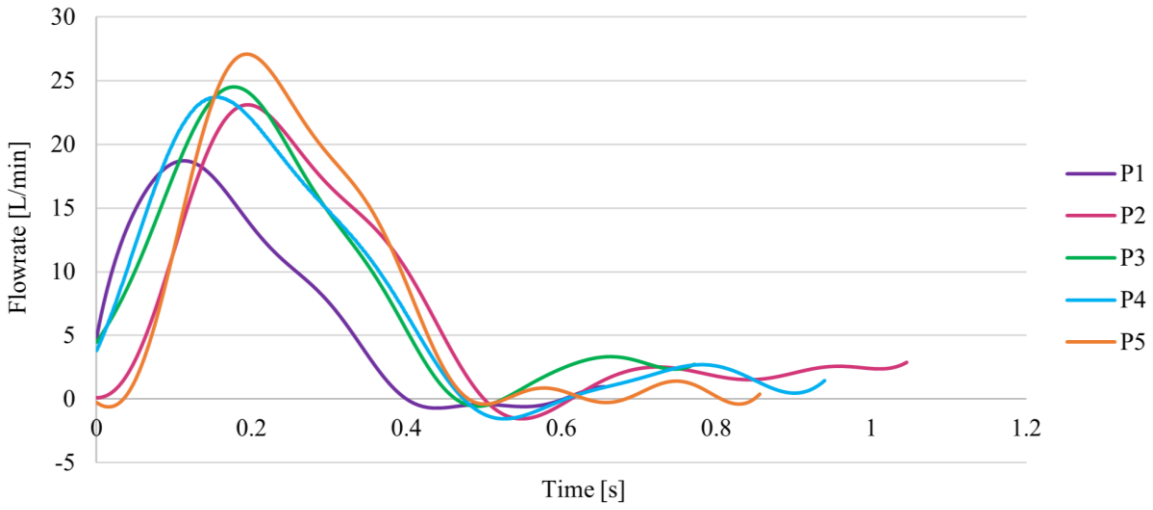

Figure 3: Inlet flow waveforms for patients P1-P5 derived from 4D-flow MRI data. [colour figure]

	BRAC	LCCA	LSA	CEL	SMA	RR	LR	RI	LI
P1									
R1 [x10^{8} Pa.s.m^{-3}]	0.9	4.4	1.2	1.8	3.7	6.0	6.7	0.5	0.5
R2 [x10^{8} Pa.s.m^{-3}]	6.9	28.0	8.9	4.0	7.5	10.0	12.0	9.5	9.7
C [x10^{-9} m^{3}.Pa^{-1}]	2.3	0.6	1.8	3.1	1.6	1.1	1.0	1.8	1.8
% inlet flow	16.3	3.6	12.3	18.6	9.6	6.7	5.7	13.7	13.5
P2									
R1 [x10^{8} Pa.s.m^{-3}]	0.3	0.9	0.6	0.8	1.1	1.3	1.4	0.4	0.3
R2 [x10^{8} Pa.s.m^{-3}]	10.8	24.8	16.6	6.5	7.8	9.3	10.0	16.6	11.4
C [x10^{-9} m^{3}.Pa^{-1}]	1.6	0.7	1.0	2.4	2.0	1.7	1.6	1.0	1.5
% inlet flow	12.2	5.3	7.9	17.4	14.3	12.0	11.3	8.0	11.6
P3									
R1 [x10^{8} Pa.s.m^{-3}]	0.4	1.3	0.6	3.3	1.8	12.2	4.9	0.6	0.3
R2 [x10^{8} Pa.s.m^{-3}]	6.9	20.6	8.9	4.6	2.9	12.3	6.2	10.9	6.8
C [x10^{-9} m^{3}.Pa^{-1}]	2.5	0.8	1.9	2.3	3.8	0.7	1.6	1.6	2.5
% inlet flow	15.2	4.9	11.2	11.8	20.1	2.9	8.5	9.5	15.9
P4									
R1 [x10^{8} Pa.s.m^{-3}]	0.5	2.1	0.8	2.3	2.9	4.9	5.4	0.5	0.8
R2 [x10^{8} Pa.s.m^{-3}]	4.4	13.8	6.4	2.0	2.4	3.2	3.7	5.2	7.3
C [x10^{-9} m^{3}.Pa^{-1}]	3.6	1.1	2.5	4.2	3.3	2.2	2.0	3.1	2.2
% inlet flow	17.7	5.1	11.8	13.9	11.9	7.6	6.7	14.9	10.4
P5									
R1 [x10^{8} Pa.s.m^{-3}]	0.5	1.9	1.0	2.8	1.5	6.6	5.0	0.3	0.3
R2 [x10^{8} Pa.s.m^{-3}]	7.9	15.5	4.6	3.6	2.2	6.9	5.6	5.1	5.2
C [x10^{-9} m^{3}.Pa^{-1}]	2.2	1.0	3.2	2.8	5.0	1.3	1.7	3.3	3.3
% inlet flow	10.4	4.5	12.9	10.4	18.6	4.8	6.2	16.3	16.0

Table 4: 3-element Windkessel parameters and percentage of inlet flow reporting to each branch in patients P1-P5. Branches include brachiocephalic (BRAC), left common carotid (LCCA) and left subclavian (LSA) artery, celiac trunk (CEL), superior mesenteric artery (SMA), right (RR) and left (LR) renal, and right (RI) and left (LI) iliac. Reported parameters are proximal resistance (R1), distal resistance (R2) and compliance (C).

27.1 L/min, and all waveforms contained a period of retrograde flow. Patients P2-P5 had a stroke volume between 113 and 117 mL while P1 had a substantially lower stroke volume of 74 mL. The cycle-averaged pressures measured from the DW waveforms recorded at the PET and thoracic and lumbar spinal locations T9, T12 and L1 (the locations of which are shown in Figure 2) can be found later in Figure 6, while systolic and diastolic pressure values at these locations are reported in Appendix B in the supplementary material. P1, P2 and P3 had systolic pressures greater than 125 mmHg throughout the aorta, while P4 and P5 presented with lower pressures (systolic values ranging from 74 to 90 mmHg).

3.3. 3-element Windkessel parameters

Table 4 reports the 3EWK parameters for all branch outlets, calculated based on branch area, average flowrates measured from 4D-MRI data and average pressures measured from DW readings. Again, there were substantial variations among the parameters, due to the variability in

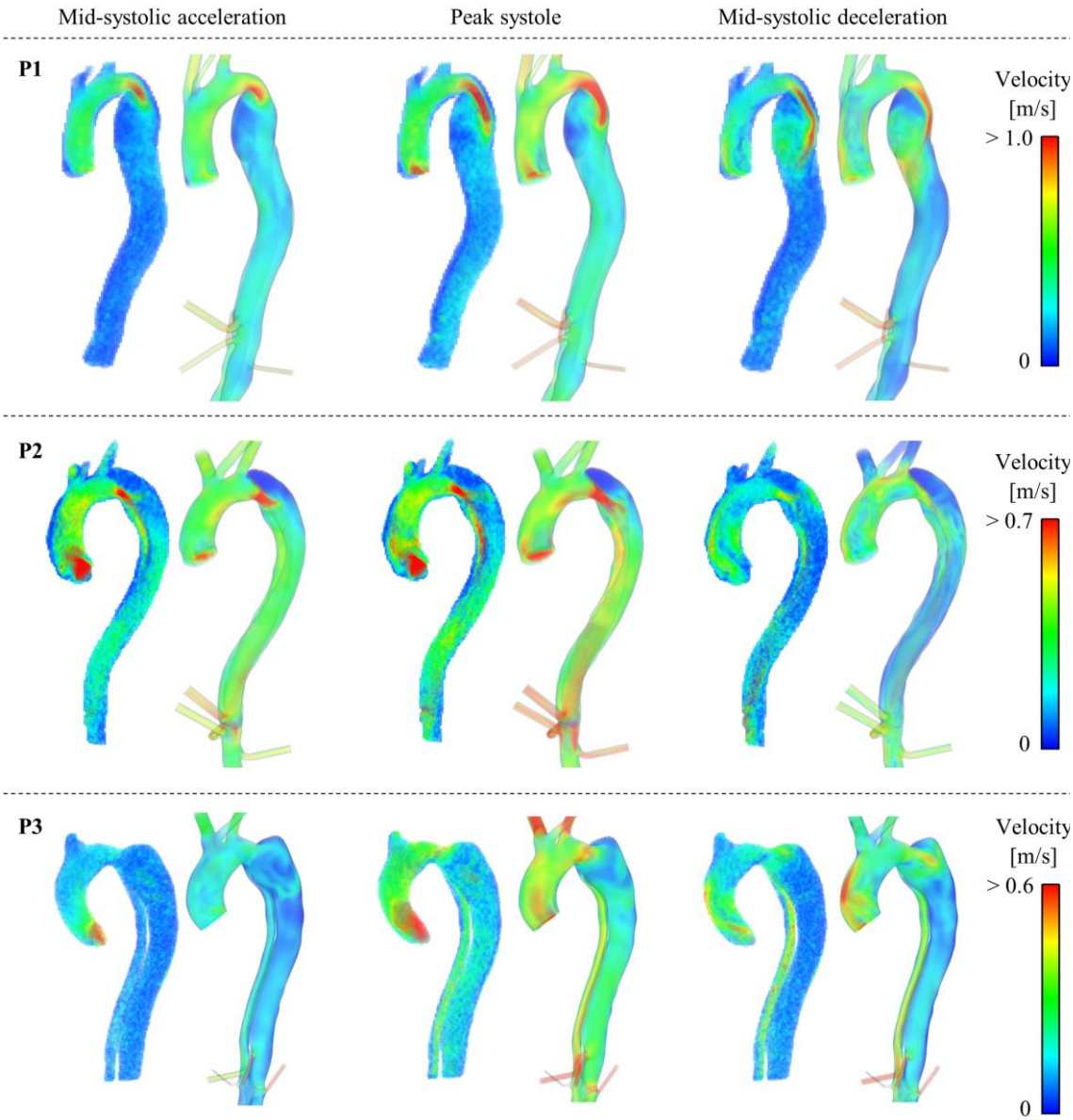

Figure 4: Mid-systolic, peak systole and mid-systolic deceleration velocity fields for P1, P2 and P3. For each patient at each time point the 4D-MRI derived velocity field is shown on the left alongside the CFD predicted velocity field on the right. [colour figure]

branch area, average flowrate and pressure inputs. Additionally, the percentage of inlet flow reporting to each branch in each patient is also presented.

3.4. Flow patterns

Figures 4 and 5 show volume renders of instantaneous velocity fields throughout the systolic phase from both the 4D-MRI data and the CFD simulations for all patients. In all cases it can be seen that there is good qualitative agreement between the simulated velocities and the *in-vivo* data. The high velocity jet through the PET in each patient was well captured both in terms of

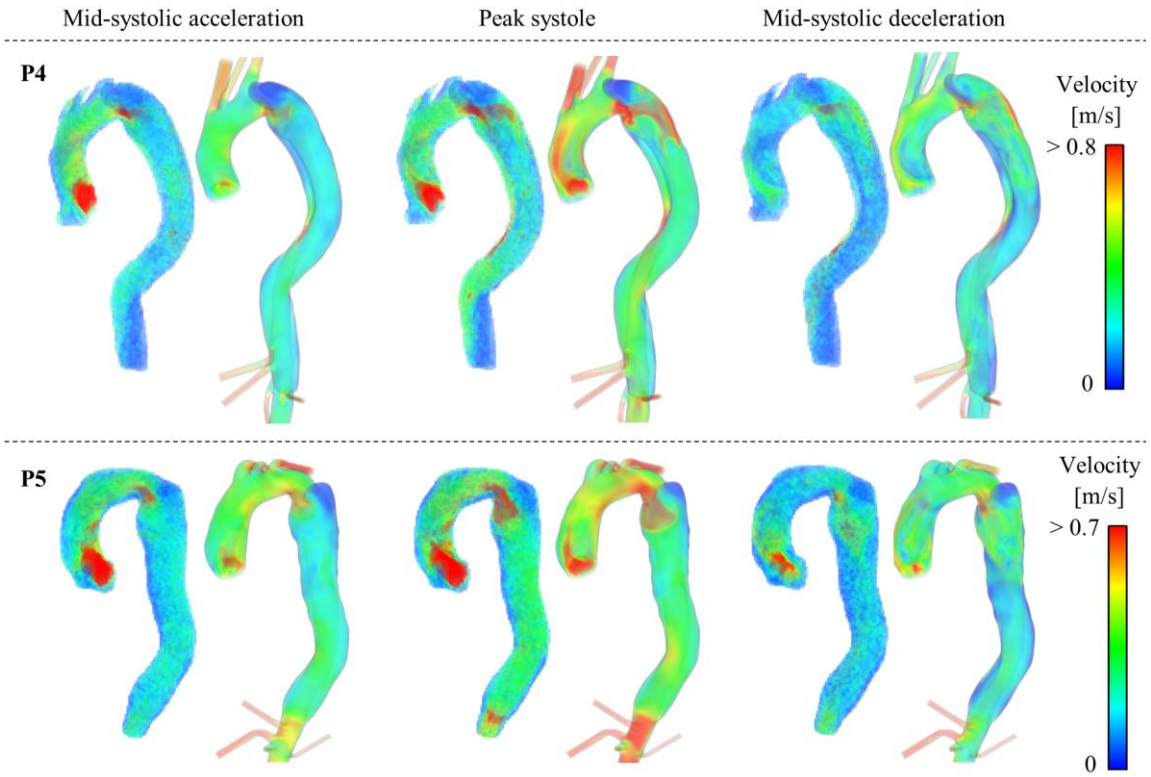

Figure 5: Mid-systolic, peak systole and mid-systolic deceleration velocity fields for P4 and P5. For each patient at each time point the 4D-MRI derived velocity field is shown on the left alongside the CFD predicted velocity field on the right. [colour figure]

magnitude and shape throughout the cardiac cycle. Generally, velocity magnitudes in the distal aorta were also well captured, with for example high TL velocities in the mid thoracic dissection of P4 both visible in the 4D-MRI data and CFD results.

Table 5 reports both the Pearson correlation coefficient (R) and the mean absolute error (MAE) between the CFD and 4D-MRI data in regions throughout the aorta, broken down into the three velocity components $\boldsymbol{u_x}$, $\boldsymbol{u_y}$ and $\boldsymbol{u_z}$. In line with the qualitative analysis, there is good agreement between the data across all patients, with weaker agreement at certain points - high positive and moderate positive correlations are defined as an R value greater than 0.7 and 0.5, respectively [40]. In the AAo, AA and Prox-DAo (regions where there are generally higher velocities and the MRI images are of better quality) 80% of the reported R values across each velocity component for all patients had an R greater than 0.5. Agreement was weaker in the Mid-DAo and Dis-DAo, where only 37% of R values were greater than 0.5. While reporting R values indicates the existence of linearity between the variables it does not indicate whether the data follows the trendline of $x = y$, which in this study is desirable, and other measures of agreement between CFD and MRI data have been presented in the literature [41]. By considering the corresponding

		AAo	AA	Prox-DAo	Mid-DAo	Dis-DAo
Pearson Correlation Coefficient (R)						
P1	u_x	0.66	0.77	0.76	0.65	0.37
	u_y	0.71	0.53	0.44	0.41	0.54
	u_z	0.72	0.71	0.44	0.30	0.18
P2	u_x	0.81	0.68	0.67	0.72	0.32
	u_y	0.66	0.63	0.66	0.64	0.42
	u_z	0.76	0.63	0.60	0.25	0.19
P3	u_x	0.69	0.78	0.64	0.38	0.28
	u_y	0.62	0.62	0.60	0.56	0.53
	u_z	0.38	0.41	0.25	0.06	0.12
P4	u_x	0.70	0.55	0.73	0.55	0.73
	u_y	0.61	0.47	0.23	0.27	0.23
	u_z	0.77	0.67	0.15	0.18	0.15
P5	u_x	0.56	0.75	0.70	0.17	0.63
	u_y	0.40	0.53	0.78	0.68	0.66
	u_z	0.58	0.72	0.53	0.22	0.25
Mean Absolute Error [m/s]						
P1	u_x	0.10	0.10	0.14	0.05	0.05
	u_y	0.17	0.16	0.22	0.11	0.12
	u_z	0.09	0.08	0.16	0.07	0.06
P2	u_x	0.11	0.12	0.13	0.07	0.12
	u_y	0.16	0.10	0.13	0.16	0.25
	u_z	0.11	0.07	0.10	0.07	0.09
P3	u_x	0.08	0.06	0.07	0.06	0.06
	u_y	0.11	0.10	0.07	0.09	0.13
	u_z	0.08	0.07	0.06	0.06	0.06
P4	u_x	0.14	0.11	0.09	0.09	0.09
	u_y	0.21	0.18	0.18	0.16	0.16
	u_z	0.14	0.08	0.11	0.10	0.10
P5	u_x	0.13	0.15	0.10	0.06	0.10
	u_y	0.21	0.11	0.11	0.09	0.11
	u_z	0.15	0.09	0.10	0.06	0.07

Table 5: Pearson correlation coefficient (R) and mean absolute error for each velocity component u_x, u_y and u_z in the 5 regions of the aorta shown in Figure 2 for all patients.

MAE for each R value reported, the general over/under estimation of velocities by the CFD compared to the 4D-MRI data can be assessed. The maximum MAE for P1-P5 was 0.22, 0.25, 0.13, 0.21 and 0.21 m/s, respectively, while the average MAE across all regions in all patients was 0.11 m/s. Neither the R value nor the MAE alone can fully describe the agreement between the data sets, thus for further detail scatter plots for each reported R value can be found in the supplementary material.

Table 6 reports the maximum peak systolic velocity and FLEF measured from the 4D-MRI data and CFD results at the PET for quantitative comparison and evaluation. In all patients the maximum velocity was well predicted by the CFD simulations, with a maximum error of 0.31 m/s in P2. All CFD maximum velocities were lower than their relative 4D-MRI measured velocities. In P1 and P5 varying levels of FLEF were measured in the 4D-MRI and the CFD correctly predicted

	P1	P2	P3	P4	P5
			Maximum PET Velocity [m/s]		
4D-MRI	1.8	1.2	0.9	1.7	1.2
CFD	1.6	0.9	0.6	1.6	1.2
			FLEF (%)		
4D-MRI	10.7	0.8	0	0	3.6
CFD	11.1	14.6	0	0	6.4

Table 6: Maximum peak systolic primary entry tear (PET) velocity and false lumen ejection fraction (FLEF, defined in equation 2 measured from 4D-flow MRI scan and predicted from CFD simulation for each patient.

these patterns, particularly well in P1. In P3 and P4 there was no reverse flow at the PET, equating to a FLEF of zero, and this was again correctly predicted in the CFD simulation. In P2 a very low FLEF of 0.8% was measured from the 4D-MRI data while the CFD predicted an FLEF of 14.6%. Reasons for this discrepancy will be explained later.

3.5. Pressure

Figure 6 presents average pressures (averaged over the cardiac cycle) at various locations throughout the aorta (in the ascending aorta, and in the TL and FL at the PET and throughout the dissection at the thoracic and lumbar spinal locations T9, T12 and L1, the location of which are indicated in Figure 2) for both invasive DW measured values and CFD predicted values for all patients. From the bar charts it can be seen that average pressures were generally well captured for all patients, with differences of less than 15% between DW and CFD values. Corresponding systolic and diastolic values at the same locations for both DW and CFD are reported in Appendix B in the supplementary material. P2 and P3 had the strongest agreement between DW and CFD within the dissection, with a maximum error of 7 mmHg at systolic TL-L1 for P2 and 9mmHg at systolic TL-PET for P3, while diastolic values were better matched throughout the dissection. However, there were significant errors in absolute systolic and diastolic values across the remaining patients. P1, P4 and P5 saw maximum errors of 36, 20 and 24 mmHg. P1 had larger systolic errors while P4 and P5 had larger diastolic errors.

Furthermore, significant TL/FL cross-lumen pressure differences measured by the DW were not predicted by the CFD simulations, the largest being in P1 where a cross-lumen pressure difference at this time and spatial point. The largest cross-lumen pressure difference predicted by CFD was 8 mmHg, at the PET of P4. Of course, individual time points are likely to have larger variations and it can be seen that using average values the largest cross-lumen pressure

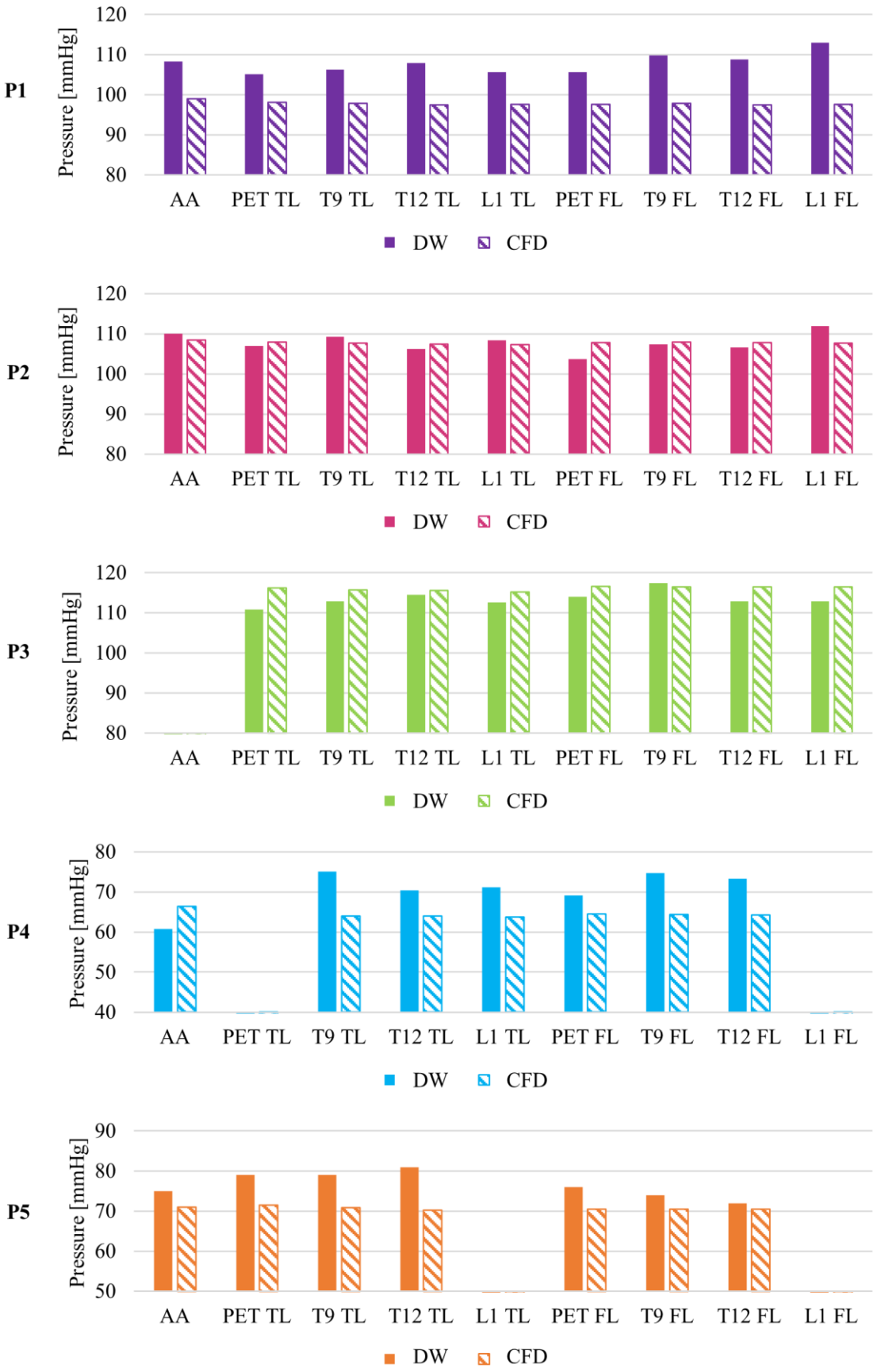

Figure 6: Doppler-wire (DW) measured and CFD predicted pressures averaged over the cardiac cycle at different locations along the aorta. Ascending aorta (AA); true (TL) and false (FL) lumen; primary entry tear (PET); spine vertebrae locations (T9/T12/L1). DW pressure curves were not available for P3 AA, P4 TL-PET and P4 FL-L1, and the dissection in P5 did not extend to L1, thus results are not reported in these regions. [colour figure]

difference recorded with the DW was 9 mmHg in P5 at T12, while nearly all other locations across all patients had an average cross-lumen pressure difference less than 5 mmHg.

In total, pressure was evaluated at 43 spatial points among the five patients. At 35 of the points the pulse pressure (defined as the systolic pressure minus the diastolic pressure) was higher with the CFD values compared to the DW pressure readings. The points where this was not the case were in the FL of P1 where systolic pressures were significantly underestimated by CFD, and the TL of P2 where PP values were close but slightly higher with the DW readings.

4. Discussion

Computational fluid dynamics simulations of TBAD have been adopted by various research groups to gain an understanding of the complex hemodynamics of the disease, and to provide a mechanistic understanding for various disease progressions. Many different studies of varying complexity [12-25] have been presented and current best methodological practices in terms of inlet [30] and outlet [29] boundary conditions have been explored. This study aimed to evaluate a fully patient-specific workflow by simulating 5 TBAD geometries, utilising the maximum amount of *in vivo* anatomical (CT scans) and flow data (4D-MRI scans and invasive DW pressure readings) that can be obtained.

As seen by the geometric data reported in Table 2 all five TBAD patients presented with dissections that varied in terms of tortuosity, TL/FL configuration, and dissection length. The patients also showed variations in the size of aortic branches (reported in Table 3). Notable differences included large branch diameters in P2, likely due to a generally larger aorta given the consistent higher than standard value across all branches. Individual branches that were abnormally small compared to the other patients and standard values included the LCCA in P1 and the RR in P3, possibly due to malperfusion.

The patients also presented with varying measured hemodynamics in terms of inlet flow waveforms and pressure values. P2-P5 all had a stroke volume within the normal range of 94±15 mL [42], while P1 at 74 mL was slightly below the lower limit of the normal range. The systolic

phase accounted for between 48% and 61% of the cardiac cycle for all patients, with similar waveforms that differed in their peak value and period.

3EWK parameters were calculated (Table 4) for each branch in all patients using the average flowrate to each branch determined from the 4D-MRI data and the average pressure determined from the DW pressure measurements taken during the TEVAR procedure. The branch diameter was also taken into account both as a required value to calculate R1 but also due to the fact that the abdominal flow measured from the 4D-MRI scan was split between the branches based on their area. Given the individual data that was input to determine the 3EWK parameters the resulting values for each patient also significantly varied.

Since 4D-flow MRI is not usually required for clinical diagnosis of aortic dissection, it is common that patient-specific flow data are not available, and boundary conditions are therefore often taken from literature in such cases. The data presented in this study (branch diameters and 3EWK parameters) provides multiple new sets of parameters which can be used in future studies. If researchers only have a CT scan, geometric features from that CT scan can be compared to the five patients presented here (number of tears, branch diameters etc) and corresponding simulation parameters can then be selected that best match the available information. R1 and R2 values can be used directly, or total resistance can be calculated as the sum of R1 and R2, with a new ratio of R1 and R2 determined using the workflow described by Pirola et al. [20]. Figure 3 also provides multiple inlet flow waveforms which can be used directly, or if any basic flow information such as heart rate or stroke volume is available, the inlet flow waveforms can be scaled to match such data.

The five patients in this study were simulated and the CFD results were compared to processed 4D-MRI data in order to validate the workflow. CFD predicted velocity fields showed good agreement to the *in vivo* flow data for all patients (Figures 4 and 5), in particular the shape and size of the high velocity jet through the PET in each patient was well captured by the CFD model. Global quantitative analysis demonstrated the agreement between the CFD and 4D-MRI velocity data through the Pearson correlation coefficients. Generally, stronger correlations were seen in the AAO, AA and Prox-DAo compared to the Mid-DAo and Dis-DAo across the patients. Due to

the small channels and lower velocities in the Mid-DAo and DisDAo the 4D-MRI was of poorer quality in these regions, meaning measured velocities likely have a higher error and the registration process required to spatially match the CT and 4D-MRI geometries for comparison is more challenging. However, the dominant direction of flow ($\boldsymbol{u_x}$ or $\boldsymbol{u_y}$ depending on the geometry orientation) mostly still saw reasonable correlations greater than 0.5, while the non-dominant components (mainly $\boldsymbol{u_z}$) had the lowest R values. Generally the R values found in this study are in line with values reported in previous studies: R = 0.64-0.92 in a healthy patient [36]; R=0.63 in an idealised aortic aneurysm geometry [37]; and R=0.74-0.87 in an ascending aorta aneurysm patient [35].

Local quantitative analysis (Table 6) showed that the velocity magnitude in the PET was well matched between the CFD and 4D-MRI results, with the largest error of 0.3 m/s in P2 and P3. The PET velocity was underestimated in all patients compared to the 4D-MRI derived value, and this was the case in previous studies [20,30]. Interestingly, the 4D-MRI data reported a higher maximum velocity in the PET region, while generally throughout the aorta on average the CFD predicted higher velocities, particularly in the AAo and AA.

There may be two sources of error causing the discrepancies in velocity results between the CFD and 4D-MRI data which relate to the relatively low image quality of the 4D-MRI scan. The first being that the size of the smaller branches (including the LCCA) is on a comparable scale to the voxel size of the scan (1.875 x 1.875 x 2.5 mm^3 for all patients) which may cause inaccuracy in measured flow, thus the estimated flow to the arch branches may be higher than is actually true, resulting in slightly less flow entering the descending aorta and through the tear. The second is the potential error in the extracted inlet velocity profile. Both abnormally high and low velocities may not be fully captured as the scan parameters (such as the velocity encoding (VENC) which dictates the range of velocities that are accurately captured) are set to minimise scan time in the clinical setting for the benefit of the patient. The use of dual VENC which repeats the scan to record a lower and higher velocity range can help to overcome this potential error source [43-45], however this is challenging in the clinical setting as it requires significantly longer scan time. Furthermore, the lower image quality means that there is some variation in the flowrate extracted depending on the location at which the plane is placed. To evaluate the likely extent of this error,

3 planes were placed near the aortic root in P1, 5 mm apart, with plane 1 closest to the aorta valve, plane 2 distal to plane 1 and still within the velocity jet, and plane 3 most distal to the valve and just slightly distal to the tip of the high velocity jet. The peak and average flowrates and stroke volume derived from plane 2 differed by a small 1.5%, -3.2% and -2.7%, respectively, compared to plane 1, while the peak and average flowrates and stroke volume derived from plane 3 differed by -11.2%, -10.3% and -8.9%, respectively, compared to plane 1. This error was minimised across all simulations by ensuring the plane placed to extract the inlet velocity profiles was set well within the high velocity jet, however, some degree of error in the final inlet velocity profiles was likely to exist. Both of these sources of error may have resulted in a slightly lower than true stroke volume being applied in the CFD simulation. The work of Armour et al. [30] showed the significant impact a reduced stroke volume can have on hemodynamic results, with a 25% reduction in stroke volume resulting in up to 28% and 35% reductions in velocity and wall shear stress, respectively. However, the results of this study suggest that any stroke volume error was likely small as there was no major deviation in velocity fields according to the quantitative and qualitative analysis which showed local regions of altered velocity patterns were still well captured by the CFD, such as the area of high velocity in the mid-thoracic TL of P4 at mid-systolic deceleration and the increased velocity around the abdominal branches of P5 at peak systole. Bozzi et al. [46] reported that deviations of ±18% in the mean inlet velocity caused significant changes in pressure and wall shear stress results, which may explain the larger deviation in predicted pressures compared to the DW measured values.

As well as velocities, flow patterns (Table 6) were well captured by the CFD simulations compared to the *in vivo* data. The lack of any flow reversal (represented by FLEF) at the PET in P3 and P4 was correctly predicted by the CFD, and the varying levels of FLEF in P1 and P5 were also in line with 4D-MRI results. The FLEF results for P2 were not consistent, with a significant over-prediction by the CFD simulation. On the CT scan for P2 there is clear motion artefact around the PET which is shown in Figure 7 - this is commonly observed on dissection CT images given the scan captures a static image but the aorta and intimal flap are mobile. This means that during segmentation there was likely some degree of error relating to the exact shape and size of the PET, and any deviation from the true geometry will impact flow through the tear, thus this is likely the source of the FLEF error in this case.

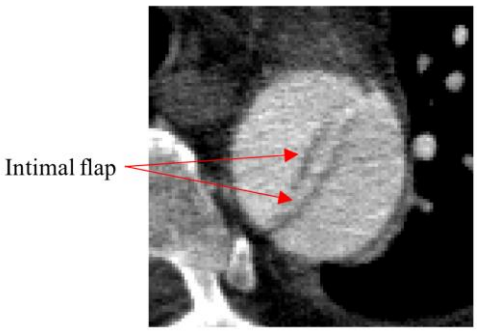

Figure 7: Motion artefact visible due to flap motion on the axial view of the descending aorta on the CT scan for P2. Red arrows indicate the intimal flap (darker line in the middle of the aorta). [colour figure]

CFD predicted pressures were compared to the *in vivo* DW measurements to evaluate agreement (Figure 6). Average pressures predicted by the CFD were in a reasonable agreement with the DW values, meaning the general pressure environment and extent of pressure elevation was captured. However, there were significant errors both in terms of absolute systolic and diastolic values. There are several factors that may contribute to these errors, the first being variation in the time at which scans and pressure measurements were taken. The DW measurements were taken during the TEVAR procedure, before the stent-graft was deployed, which would have been on a different day to when the diagnostic CT and 4D-flow MRI scans were taken. It is known that dissections can progress rapidly in the acute phase, including stiffening of the intimal flap [47]. Any progression of the disease between the diagnostic scan and TEVAR procedure may have resulted in varied pressure and flow fields within the aorta. Armour et al. [30] showed the significant impact peak systolic inlet flowrate and general flow waveform can have on predicted pressures, and therefore change due to disease progression may result in different flow splits and therefore cross-lumen pressure differences.

Another factor that may contribute to the error in systolic and diastolic values is the way in which the pressure data is used to tune the 3-EWK parameters. It can be seen from the methodology presented by Pirola et al. [20] that to calculate the 3-EWK parameters average flow and average pressure at each branch is required. To do this, the average pressure measured from the DW pressure curve is calculated and utilised. The pressure at each branch is initialised with the corresponding measured diastolic value, however there is no point in the methodology where the maximum systolic pressure is taken into account. This may explain why the CFD simulations do

predict the average pressures in the aorta, but often miss the extreme maximum value in the cardiac cycle.

Moreover, while invasive DW pressure measurements are considered the gold-standard there is likely still some degree of error in these readings themselves. Discussions with our collaborators who conducted the surgeries in which the pressure readings were taken highlighted potential error sources. In dissections the TL and FL can at times be very narrow, and with the highly mobile intimal flap early on in the disease it is possible that flap motion may cause the DW tip to come into contact with the tissue thus influencing the pressure reading. Furthermore, the geometry of dissections means there are often areas of high velocity and complex flow patterns, particularly around tears - a clear example of which can be seen in the PET in all patients in Figures 4 and 5. This makes it challenging to achieve a steady reading on the DW. In this case the reading may be taken multiple times and averaged to minimise the error however to reduce the surgery time this is not always possible.

Finally, the rigid wall assumption in these simulations is a key limitation and likely impacted the pressure results. Recent work using an idealised geometry by Chong et al. [48] showed that rigid wall simulations can overestimate systolic pressures and underestimate diastolic pressures and therefore overestimate pulse pressure. It was seen that in most cases the pulse pressure was overestimated by the CFD simulations in this study, and wall and flap motion may rectify this to bring the pulse pressures more in line with the DW readings. A patient-specific study by Bäumler et al. [49] showed that rigid simulations can overestimate cross-lumen pressure differences. Given the rigid simulations in this study generally underestimated cross-lumen pressure differences compared to DW readings it is unclear if wall motion would account for this error given the conclusion of Bäumler et al. [49] would suggest inclusion of wall motion would further decrease this pressure difference. A recent study by Zimmermann et al. [50] combined experimental and computational methods in which a patient-specific TBAD model was 3D printed and embedded in a physiological flow circuit. Pressure measurements were then taken within the experimental aorta and a 4D-MRI scan of the set up was also taken. A fluid-structure interactions (FSI) simulation of the patient-specific model was then carried out and the results showed accurate prediction of the cross-lumen pressure difference at multiple locations in the dissection. The

catheter pressure readings and 4D-MRI flow scan are expected to be of better quality than the *in vivo* data of the current study, given the controlled experimental condition, but the well matched CFD pressure results indicate the importance of flap and wall motion. For clarity and further understanding, fully coupled FSI simulations should be carried out in the future to allow for the impact of the rigid wall assumption to be properly evaluated. A major barrier here is the lack of material properties of TBAD due to the scarce availability of dissected aortic tissues for mechanical testing. However, recent studies by Amabili et al. [51] of a chronic type A dissection and Kan et al. [52] of type B aortic dissections provided valuable biomechanical details on which material property models can be built.

5. Conclusions

This study presents CFD simulations of five TBAD patients, following a workflow that incorporated the maximum amount of anatomical and flow data that can be acquired *in vivo*: patient-specific geometries from CT scans, 3D inlet velocity profiles and outlet flowrates derived from 4D-flow MRI, and DW pressure measurements. The patients presented with varying dissection geometries and differing aortic branch sizes, resulting in a range of 3-EWK parameters which have been presented here. This data can be utilised in future studies where researchers do not have patient-specific flow data to tune 3EWK parameters, but want to implement values which represent the studied geometry. The CFD results were evaluated and compared with the processed 4D-MRI scans, and strong agreement in flow patterns and velocity magnitudes throughout the cardiac cycle was seen in all patients. CFD predicted pressures were compared against DW measurements, and average pressures were generally well predicted within an acceptable margin of error for all patients, however there were errors in the CFD predicted instantaneous systolic and diastolic pressures, and cross-lumen pressure differences were generally underestimated by the CFD, all of which should be investigated further with FSI studies.

Conflict of interest statement

None declared.

Funding

This work was supported in part by the National Natural Science Foundation of China [82000436, 81770474, 81770508]; Shanghai Committee of Science and Technology, China [201409004800]; a PhD scholarship award to CHA through Engineering and Physical Sciences Research Council Doctoral Training Partnership grant to Imperial College London [EP/R512540/1]; and the Royal Society, UK [IE161052].

References

[1] Salameh, M. J., & Ratchford, E. V. (2016). Aortic Dissection. *Vascular Medicine*, *21*(3), 276–280. https://doi.org/10.1177/1358863X16632898

[2] Pape, L. A., Awais, M., Woznicki, E. M., Suzuki, T., Trimarchi, S., Evangelista, A., Myrmel, T., Larsen, M., Harris, K. M., Greason, K., Di Eusanio, M., Bossone, E., Montgomery, D. G., Eagle, K. A., Nienaber, C. A., Isselbacher, E. M., & O'Gara, P. (2015). Presentation, diagnosis, and outcomes of acute aortic dissection: 17-year trends from the international registry of acute aortic dissection. *Journal of the American College of Cardiology*, *66*(350–358). https://doi.org/10.1016/j.jacc.2015.05.029

[3] Evangelista, A., Salas, A., Ribera, A., Ferreira-González, I., Cuellar, H., Pineda, V., González-Alujas, T., Bijnens, B., Permanyer-Miralda, G., & Garcia-Dorado, D. (2012). Long-term outcome of aortic dissection with patent false lumen: Predictive role of entry tear size and location. *Circulation*, *125*, 3133–3141. https://doi.org/10.1161/CIRCULATIONAHA.111.090266

[4] Kotelis, D., Grebe, G., Kraus, P., Müller-Eschner, M., Bischoff, M., von Tengg-Kobligk, H., & Böckler, D. (2016). Morphologic predictors of aortic expansion in chronic type B aortic dissection. *Vascular*, *24*(2), 187–193. https://doi.org/10.1177/1708538115591941

[5] Kitamura, T., Torii, S., Oka, N., Horai, T., Itatani, K., Yoshii, T., Nakamura, Y., Shibata, M., Tamura, T., Araki, H., Matsunaga, Y., Sato, H., & Miyaji, K. (2015). Impact of the entry site on late outcome in acute Stanford type B aortic dissection. *European Journal of Cardio-Thoracic Surgery*, *48*(5), 655–661. https://doi.org/10.1093/ejcts/ezu531

[6] Marui, A., Mochizuki, T., Koyama, T., & Mitsui, N. (2007). Degree of fusiform dilatation of the proximal descending aorta in type B acute aortic dissection can predict late aortic events.

Journal of Thoracic and Cardiovascular Surgery, *134*(5), 1163–1170. https://doi.org/10.1016/j.jtcvs.2007.07.037

[7] Ray, H. M., Durham, C. A., Ocazionez, D., Charlton-Ouw, K. M., Estrera, A. L., Miller, C. C., Safi, H. J., & Azizzadeh, A. (2016). Predictors of intervention and mortality in patients with uncomplicated acute type B aortic dissection. *Journal of Vascular Surgery*, *64*(6), 1560–1568. https://doi.org/10.1016/j.jvs.2016.07.111

[8] Sailer, A. M., Van Kuijk, S. M. J., Nelemans, P. J., Chin, A. S., Kino, A., Huininga, M., Schmidt, J., Mistelbauer, G., Bäumler, K., Chiu, P., Fischbein, M. P., Dake, M. D., Miller, D. C., Schurink, G. W. H., & Fleischmann, D. (2017). Computed Tomography Imaging Features in Acute Uncomplicated Stanford Type-B Aortic Dissection Predict Late Adverse Events. *Circulation: Cardiovascular Imaging*, *10*(4), 1–11. https://doi.org/10.1161/CIRCIMAGING.116.005709

[9] Spinelli, D., Benedetto, F., Donato, R., Piffaretti, G., Marrocco-Trischitta, M. M., Patel, H. J., Eagle, K. A., & Trimarchi, S. (2018). Current evidence in predictors of aortic growth and events in acute type B aortic dissection. *Journal of Vascular Surgery*, *68*(6), 1925-1935.e8. https://doi.org/10.1016/j.jvs.2018.05.232

[10] Tolenaar, J. L., Van Keulen, J. W., Jonker, F. H. W., Van Herwaarden, J. A., Verhagen, H. J., Moll, F. L., Muhs, B. E., & Trimarchi, S. (2013). Morphologic predictors of aortic dilatation in type B aortic dissection. *Journal of Vascular Surgery*, *58*(5), 1220–1225. https://doi.org/10.1016/j.jvs.2013.05.031

[11] Tolenaar, J. L., Van Keulen, J. W., Trimarchi, S., Jonker, F. H. W., Van Herwaarden, J. A., Verhagen, H. J. M., Moll, F. L., & Muhs, B. E. (2013). Number of entry tears is associated with aortic growth in type B dissections. *Annals of Thoracic Surgery*, *96*(1), 39–42. https://doi.org/10.1016/j.athoracsur.2013.03.087

[12] Alimohammadi, M., Agu, O., Balabani, S., & Díaz-Zuccarini, V. (2014). Development of a patient-specific simulation tool to analyse aortic dissections: Assessment of mixed patient-specific flow and pressure boundary conditions. *Medical Engineering and Physics*, *36*(3), 275–284. https://doi.org/10.1016/j.medengphy.2013.11.003

[13] Bonfanti, M., Franzetti, G., Maritati, G., Homer-Vanniasinkam, S., Balabani, S., & Díaz-Zuccarini, V. (2019). Patient-specific haemodynamic simulations of complex aortic dissections informed by commonly available clinical datasets. *Medical Engineering and Physics*, *71*, 45–55. https://doi.org/10.1016/j.medengphy.2019.06.012

[14] Cheng, Z., Tan, F. P. P., Riga, C. V., Bicknell, C. D., Hamady, M. S., Gibbs, R. G. J., Wood, N. B., & Xu, X. Y. (2010). Analysis of Flow Patterns in a Patient-Specific Aortic Dissection Model. *Journal of Biomechanical Engineering*. https://doi.org/10.1115/1.4000964

[15] Cheng, Z., Riga, C., Chan, J., Hamady, M., Wood, N. B., Cheshire, N. J. W., Xu, Y., & Gibbs, R. G. J. (2013). Initial findings and potential applicability of computational simulation of the aorta in acute type B dissection. *Journal of Vascular Surgery*, *57*, 35S-43S. https://doi.org/10.1016/j.jvs.2012.07.061

[16] Cheng, Z., Wood, N. B., Gibbs, R. G. J., & Xu, X. Y. (2014). Geometric and Flow Features of Type B Aortic Dissection: Initial Findings and Comparison of Medically Treated and Stented Cases. *Annals of Biomedical Engineering*, *43*(1), 177–189. https://doi.org/10.1007/s10439-014-1075-8

[17] Cheng, Z., Juli, C., Wood, N. B., Gibbs, R. G. J., & Xu, X. Y. (2014). Predicting flow in aortic dissection: Comparison of computational model with PC-MRI velocity measurements. *Medical Engineering and Physics*, *36*, 1176–1184. https://doi.org/10.1016/j.medengphy.2014.07.006

[18] Dillon-Murphy, D., Noorani, A., Nordsletten, D., & Figueroa, C. A. (2016). Multi-modality image-based computational analysis of haemodynamics in aortic dissection. *Biomechanics and Modeling in Mechanobiology*, *15*(4), 857–876. https://doi.org/10.1007/s10237-015-0729-2

[19] Munshi, B., Parker, L. P., Norman, P. E., & Doyle, B. J. (2020). The application of computational modeling for risk prediction in type B aortic dissection. *Journal of Vascular Surgery*, *71*(5), 1789-1801.e3. https://doi.org/10.1016/j.jvs.2019.09.032

[20] Pirola, S., Guo, B., Menichini, C., Saitta, S., Fu, W., Dong, Z., & Xu, X. Y. (2019). 4-D Flow mri-based computational analysis of blood flow in patient-specific aortic dissection. *IEEE Transactions on Biomedical Engineering*, *66*(12), 3411–3419. https://doi.org/10.1109/TBME.2019.2904885

[21] Shang, E. K., Nathan, D. P., Fairman, R. M., Bavaria, J. E., Gorman, R. C., Gorman, J. H., & Jackson, B. M. (2015). Use of computational fluid dynamics studies in predicting aneurysmal degeneration of acute type B aortic dissections. *Journal of Vascular Surgery*, *62*(2), 279–284. https://doi.org/10.1016/j.jvs.2015.02.048

[22] Sun, Z., & Chaichana, T. (2016). A systematic review of computational fluid dynamics in type B aortic dissection. *International Journal of Cardiology*, *210*, 28–31. https://doi.org/10.1016/j.ijcard.2016.02.099

[23] Tse, K. M., Chiu, P., Lee, H. P., & Ho, P. (2011). Investigation of hemodynamics in the development of dissecting aneurysm within patient-specific dissecting aneurismal aortas using computational fluid dynamics (CFD) simulations. *Journal of Biomechanics*, *44*(5), 827–836. https://doi.org/10.1016/j.jbiomech.2010.12.014

[24] Wan Ab Naim, W. N., Ganesan, P. B., Sun, Z., Osman, K., & Lim, E. (2014). The impact of the number of tears in patient-specific Stanford type b aortic dissecting aneurysm: CFD simulation. *Journal of Mechanics in Medicine and Biology*, *14*(2). https://doi.org/10.1142/S0219519414500171

[25] Armour, C. H., Menichini, C., Milinis, K., Gibbs, R. G. J., & Xu, X. Y. (2020). Location of Reentry Tears Affects False Lumen Thrombosis in Aortic Dissection Following TEVAR. *Journal of Endovascular Therapy*, *27*(3), 396–404. https://doi.org/10.1177/1526602820917962

[26] Qin, Y. L., Deng, G., Li, T. X., Jing, R. W., & Teng, G. J. (2012). Risk factors of incomplete thrombosis in the false lumen after endovascular treatment of extensive acute type B aortic dissection. *Journal of Vascular Surgery*, *56*(1232–1238). https://doi.org/10.1016/j.jvs.2012.04.019

[27] Tolenaar, J. L., Kern, J. A., Jonker, F. H., Cherry, K. J., Tracci, M. C., Angle, J. F., Sabri, S., Trimarchi, S., Strider, D., Alaiwaidi, G., & Upchurch Jr, G. R. (2014). Predictors of false lumen thrombosis in type B aortic dissection treated with TEVAR. *Annals of Cardiothoracic Surgery*, *3*(3), 255–263. https://doi.org/10.3978/j.issn.2225-319X.2014.05.17

[28] Kamman, A. V., Brunkwall, J., Verhoeven, E. L., Heijmen, R. H., Trimarchi, S., Kasprzak, P., Brunkwall, J., Heijmen, R., Alric, P., Verhoeven, E., Schumacher, H., Fabiani, J. N., Eckstein, H. H., Taylor, P., Mailina, M., Mangialardi, N., Larzon, T., Böckler, D., Lönn, L., … Lammer, J. (2017). Predictors of aortic growth in uncomplicated type B aortic dissection from the Acute Dissection Stent Grafting or Best Medical Treatment (ADSORB) database. *Journal of Vascular Surgery*, *65*(4), 964–971. https://doi.org/10.1016/j.jvs.2016.09.033

[29] Pirola, S., Cheng, Z., Jarral, O. A., O'Regan, D. P., Pepper, J. R., Athanasiou, T., & Xu, X. Y. (2017). On the choice of outlet boundary conditions for patient-specific analysis of aortic flow using computational fluid dynamics. *Journal of Biomechanics*, *60*, 15–21. https://doi.org/10.1016/j.jbiomech.2017.06.005

[30] Armour, C., Guo, B., Pirola, S., Saitta, S., Liu, Y., Dong, Z., & Xu, X. Y. (2020). The influence of inlet velocity profile on predicted flow in type B aortic dissection. *Biomechanics and Modeling in Mechanobiology*, *0123456789*. https://doi.org/10.1007/s10237-020-01395-4

[31] Pirola, S., Jarral, O. A., O'Regan, D. P., Asimakopoulos, G., Anderson, J. R., Pepper, J. R., Athanasiou, T., & Xu, X. Y. (2018). Computational study of aortic hemodynamics for patients with an abnormal aortic valve: The importance of secondary flow at the ascending aorta inlet. *APL Bioengineering*, *2*(2), 026101. https://doi.org/10.1063/1.5011960

[32] Kandail, H., Hamady, M., Xu, X.Y. (2014) Patient-specific analysis of displacement forces acting on fenestrated stent grafts for endovascular aneurysm repair. *Journal of Biomechanics*, 47(14), 3546-3554.

[33] Kousera, C. A., Wood, N. B., Seed, W. A., Torii, R., O'Regan, D., & Xu, X. Y. (2012). A Numerical Study of Aortic Flow Stability and Comparison With *In Vivo* Flow Measurements. *Journal of Biomechanical Engineering*, *135*(1), 011003. https://doi.org/10.1115/1.4023132

[34] Burris, N. S., Nordsletten, D. A., Sotelo, J. A., Grogan-Kaylor, R., Houben, I. B., Figueroa, C. A., Uribe, S., & Patel, H. J. (2020). False lumen ejection fraction predicts growth in type B aortic dissection: preliminary results. *European Journal of Cardio-Thoracic Surgery : Official Journal of the European Association for Cardio-Thoracic Surgery*, *57*(5), 896–903. https://doi.org/10.1093/ejcts/ezz343

[35] Manchester, E. L., Pirola, S., Salmasi, M. Y., O'Regan, D. P., Athanasiou, T., & Xu, X. Y. (2021). Analysis of Turbulence Effects in a Patient-Specific Aorta with Aortic Valve Stenosis. *Cardiovascular Engineering and Technology*. https://doi.org/10.1007/s13239-021-00536-9

[36] Miyazaki, S., Itatani, K., Furusawa, T., Nishino, T., Sugiyama, M., Takehara, Y., & Yasukochi, S. (2017). Validation of numerical simulation methods in aortic arch using 4D Flow MRI. *Heart and Vessels*, *32*(8), 1032–1044. https://doi.org/10.1007/s00380-017-0979-2

[37] Puiseux, T., Sewonu, A., Meyrignac, O., Rousseau, H., Nicoud, F., Mendez, S., & Moreno, R. (2019). Reconciling PC-MRI and CFD: An in-vitro study. *NMR in Biomedicine*, *32*(5), 1–14. https://doi.org/10.1002/nbm.4063

[38] Du, T., Hu, D., & Cai, D. (2015). Outflow boundary conditions for blood flow in arterial trees. *PLoS ONE*, *10*(5), 1–22. https://doi.org/10.1371/journal.pone.0128597

[39] Uberoi, R., Tsetis, D., Shrivastava, V., Morgan, R., & Belli, A. M. (2011). Standard of practice for the interventional management of isolated iliac artery aneurysms. *CardioVascular and Interventional Radiology*, *34*(1), 3–13. https://doi.org/10.1007/s00270-010-0055-0

[40] Mukaka, M. M. (2012). Statistics corner: A guide to appropriate use of correlation coefficient in medical research. *Malawi Medical Journal*, *24*(3), 69–71.

[41] Wüstenhagen, C., John, K., Langner, S., Brede, M., Grundmann, S., & Bruschewski, M. (2021). CFD validation using in-vitro MRI velocity data – Methods for data matching and CFD error quantification. *Computers in Biology and Medicine*, *131*(January). https://doi.org/10.1016/j.compbiomed.2021.104230

[42] Maceira, A. M., Prasad, S. K., Khan, M., & Pennell, D. J. (2006). Reference right ventricular systolic and diastolic function normalized to age, gender and body surface area from steady-state free precession cardiovascular magnetic resonance. *European Heart Journal*, *27*(23), 2879–2888. https://doi.org/10.1093/eurheartj/ehl336

[43] Nett, E. J., Johnson, K. M., Frydrychowicz, A., Del Rio, A. M., Schrauben, E., Francois, C. J., & Wieben, O. (2012). Four-dimensional phase contrast MRI with accelerated dual velocity encoding. *Journal of Magnetic Resonance Imaging*, *35*(6), 1462–1471. https://doi.org/10.1002/jmri.23588

[44] Ha, H., Kim, G. B., Kweon, J., Kim, Y. H., Kim, N., Yang, D. H., & Lee, S. J. (2016). Multi-VENC acquisition of four-dimensional phase-contrast MRI to improve precision of velocity field measurement. *Magnetic Resonance in Medicine*, *75*(5), 1909–1919. https://doi.org/10.1002/mrm.25715

[45] Concannon, J., Hynes, N., McMullen, M., Smyth, E., Moerman, K., McHugh, P. E., Sultan, S., Karmonik, C., & McGarry, J. P. (2020). A Dual-VENC Four-Dimensional Flow MRI Framework for Analysis of Subject-Specific Heterogeneous Nonlinear Vessel Deformation. *Journal of Biomechanical Engineering*, *142*(11), 1–15. https://doi.org/10.1115/1.4048649

[46] Bozzi, S., Morbiducci, U., Gallo, D., Ponzini, R., Rizzo, G., Bignardi, C., & Passoni, G. (2017). Uncertainty propagation of phase contrast-MRI derived inlet boundary conditions in computational hemodynamics models of thoracic aorta. *Computer Methods in Biomechanics and Biomedical Engineering*, *20*(10), 1104–1112. https://doi.org/10.1080/10255842.2017.1334770

[47] Peterss, S., Mansour, A. M., Ross, J. A., Vaitkeviciute, I., Charilaou, P., Dumfarth, J., Fang, H., Ziganshin, B. A., Rizzo, J. A., Adeniran, A. J., & Elefteriades, J. A. (2016). Changing Pathology of the Thoracic Aorta From Acute to Chronic Dissection: Literature Review and Insights. *Journal of the American College of Cardiology*, *68*(10), 1054–1065. https://doi.org/10.1016/j.jacc.2016.05.091

[48] Chong, M. Y., Gu, B., Chan, B. T., Ong, Z. C., Xu, X. Y., & Lim, E. (2020). Effect of intimal flap motion on flow in acute type B aortic dissection by using fluid-structure interaction. *International Journal for Numerical Methods in Biomedical Engineering*, *36*(12), 1–22. https://doi.org/10.1002/cnm.3399

[49] Bäumler, K., Vedula, V., Sailer, A. M., Seo, J., Chiu, P., Mistelbauer, G., Chan, F. P., Fischbein, M. P., Marsden, A. L., & Fleischmann, D. (2020). Fluid–structure interaction simulations of patient-specific aortic dissection. *Biomechanics and Modeling in Mechanobiology*, *0123456789*. https://doi.org/10.1007/s10237-020-01294-8

[50] Zimmermann, J., Baeumler, K., Loecher, M., Cork, T. E., Kolawole, F. O., Gifford, K., Marsden, A. L., Fleischmann, D., & Ennis, D. B. (2021). Quantitative Hemodynamics in Aortic Dissection: Comparing in vitro MRI with FSI Simulation in a Compliant Model. 1–8. http://arxiv.org/abs/2102.13213

[51] Amabili, M., Arena, G.E., Balasubramanian, P., Breslavsky, I.D., Cartier, R., Ferrari, G., Holzapfel, G.A., Kassab, A., Mongrain, R. (2020). Biomechanical characterization of a chronic type a dissected human aorta. *Journal of Biomechanics,* 110, 109978 https://doi.org/10.1016/j.jbiomech.2020.109978

[52] Kan, X., Ma, T., Lin, J., Wang, L., Dong, Z., Xu, X.Y. (2021) Patient-specific simulation of stent-graft deployment in type B aortic dissection: model development and validation. *Biomechanics and Modeling in Mechanobiology.* https://doi.org/10.1007/s10237-021-01504-x